This is the accepted author's version of the manuscript. Final edited version can be found at: https://ieeexplore.ieee.org/document/8722759
doi: 10.1109/ROBOSOFT.2019.8722759

A robotic forearm orthosis using soft fabric-based helical actuators

Jonathan Realmuto, and Terence Sanger

***Abstract*— This article outlines the design, construction, and preliminary human-subject evaluation of a robotic forearm orthosis. The robotic forearm orthosis integrates an antagonistic pair of soft fabric-based helical actuators, which provide active pronation and supination torques. The pneumatic fabric-based helical actuators are fabricated with a knit elastic band, strain limiting nylon fabric, and internal bladder. Empirical isometric loading characteristics show that the actuators can provide up to 1.7 Nm of torque when inflated to an internal pressure of 690 kPa (100 psi). The effectiveness of torque assistance provided by the robotic forearm orthosis was assessed during a preliminary ($N = 6$) human-subjects evaluation. Subjects completed pronation and supination reaching tasks, while varying levels of assistive torque were applied to the users. Subject effort was evaluated with surface electromyography. Results indicate that the assistive torques provided by the proposed robotic orthosis significantly decreased subjects' efforts during both reaching tasks. On average, the proposed robotic orthosis reduced the effort by 59% and 24%, for supination and pronation respectively. This work demonstrates the practical implementation of a tunable fabric-based robotic forearm orthosis, that can reduce user effort during a manipulation task.**

I. Introduction

For people with movement disorders, such as Parkinson disease (PD), dystonia, tremor, and stroke induced hemiparesis, completing activities of daily living (ADLs) poses a significant challenge. Many essential ADLs, e.g., pouring from a pitcher, operating knobs, self feeding, and opening a door, require substantial forearm pronation and supination (axial rotation of the wrist) [1]. Traditional upper limb robotic orthoses (i.e., rigid exoskeletons), can provide physical therapy and/or assist in movement, thus, have the potential to enhance recovery, restore movement, and increase independence. However, rigid robotic structures are often stationary [2], have kinematic incompatibilities when the robot and human joints are misaligned [3], and can add substantial inertia to the segments of the human arm, requiring compensatory nonphysiological muscle strategies during movement [4]. In contrast, a soft robotic approach offers many advantages, such as lightweight, compliance, portability, and ease of donning/doffing, which could allow daily use and provide at home rehabilitation.

Advances in soft robotics are enabling a new generation of lightweight, compliant and versatile upper limb wearable robots. Cable driven exosuits have been shown to reduce effort during weighted elbow flexion/extension [5]. Elastomeric, fluid driven actuators, are being envisioned for hand rehabilitation [6], and elbow flexion [7]. Nevertheless, little research has been invested into soft wearable robots that assist in forearm supination/pronation. A preliminary design, incorporating two pairs of McKibben actuators that cross on both the palmar and dorsal sides of the forearm, allows for wrist flexion/extension and pronation/supination [8]. However, further investigation into soft robotic solution for forearm rotation assistance is needed.

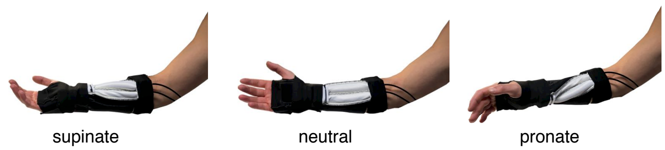

Fig. 1: Robotic forearm orthosis concept. The robotic orthosis, anchored to the user's hand and forearm with a neoprene sleeve, rigid hand and forearm support structures, and velcro straps, can assist in pronation and supination.

The ideal soft actuator for wearable robotic systems is unclear. Elastomer-based actuators, such as pneu-nets and fiber-reinforced actuators, can achieve complex motions, such as bending, twisting and extending [9], [10]. However, due to material stiffness and weight, these actuators are not ideal for on-body applications. Alternatively, textiles, which are lightweight and conformable, offer unique structural properties than can be exploited, for example, to achieve torsion [11] and spring-like mechanics [12]. Indeed, fabric-based actuators are emerging as a attractive technology for soft wearable robots [13]–[16]. One promising direction is combining anisotropic fabrics with straining limiting fabrics, which when inflated can produce motion [16]. Similar to elastomeric-based actuators, the principle of anisotropic fabric-based actuation is the deformation of compliant regions of the actuators, through the injection of a compressed fluid. Although promising, the technology is immature, with only bending and extending demonstrated thus far.

Therefore, the aim of this work is to investigate the use of fabric-based actuators for driving a robotic forearm orthosis. We extend the methods in [16], to produce fabric-based actuator capable of helical motions. We argue that, due to the biomechanics of forearm rotation, helical actuators are ideal for delivering pronation/supination torque. The robotic orthosis, shown in Fig. 1, is constructed by attaching two opposing (antagonistic) helical actuators, onto a wearable artifact, which is secured to the wrist, hand and forearm using rigid inserts. We hypothesize that, for tasks requiring forearm rotation, an increase in torque assistance will decrease user's effort.

*This work was supported by the Crowley Carter Foundation.

J. Realmuto is with the Department of Biomedical Engineering, University of Southern California. realmuto@usc.edu

T. Sanger is with Faculty of Biomedical Engineering, Biokinesiology, and Child Neurology, University of Southern California. terry@sangerlab.net

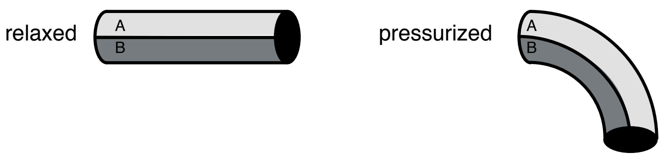

Fig. 2: Conceptualization of fabric-based bending actuators. If material-A can strain longitudinally, while material-B is inextensible, then when the (sealed) cylinder is pressurized, material-A will elongate, while material B will remain fixed, resulting in bending.

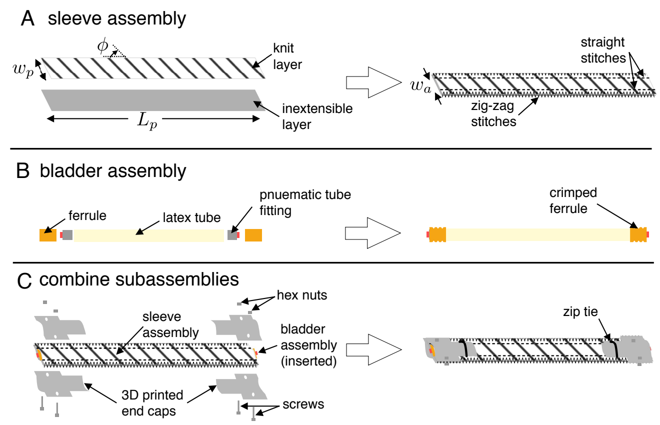

Fig. 3: Fabrication procedure for fabric-based helical actuators. **(A)** The sleeve is assembled with rectangular patterns (length L_p and width w_p) of an anisotropic top layer (knit angle ϕ) and strain-limiting bottom layer, which are sewn together with a zig-zag edge stitch. Two parallel straight stitches (width w_a) are sewn to form the pocket for the bladder. **(B)** The bladder is assembled with two push-to-connect tube fittings inserted into the tube at both ends and secured by crimped hose ferules. **(C)** The actuator is completed by inserting the bladder assembly into the sleeve and securing ends with 3D printed caps using screws and zip-ties.

II. Fabric-based Helical Actuators

A. Qualitative description of the actuation principle

The motion of the proposed soft actuator is achieved through the deformation of compliant regions of the actuator structure through the injection of compressed air. Our method is adopted from [16], and combines fabrics with different material properties, constraining deformation to a pre-programmed direction. To conceptualize the mechanics, consider a hollow cylinder (ends sealed) composed of two thin materials (Fig. 2). If both materials are isotropically inextensible, then inflating the cylinder (i.e., with compressed air) will cause it to become more rigid [12]. However, if one material (i.e., material-A in Fig. 2) can strain along the longitudinal axis, but remains inextensible in the orthogonal (radial) direction, then pressurizing the cylinder will cause it to lengthen longitudinally, while the length of the *strain-limiting* material (i.e., material-B) remains fixed, resulting in bending. Let ϕ denote the angle between the principle strain axis of the anisotropic material and the longitudinal axis of the actuator. If $\phi = 0°$, then when inflated, bending will be achieved, as outlined above. If $\phi = 90°$, then inflation will cause radial expansion of the anisotropic layer, resulting in rigidization with no longitudinal length change. However, if the angle $\phi \in (0°, 90°)$, helical motions are realized.

B. Fabrication

Stage one of the fabrication process is illustrated in 3**A**. The anisotropic layer is chosen as a knit elastic band (Cisone, 6 Inches Wide White Heavy Stretch High Elasticity Knit Elastic Band), typically used as waistbands in garments. For the strain-limiting fabric, a ballistic nylon (Magna Fabrics, 1050 Denier Coated Ballistic Nylon Fabric) is used. Prior to pattern cutting, the knit elastic band must be aligned with the chosen knit angle ϕ. The actuator sleeve, which is composed of the two fabrics, is constructed by cutting rectangular patterns (in our case length $L_p = 19$ cm, width $w_p = 4$ cm) from their respective materials. Next, the rectangular patterns are sewn together, at the two longitudinal edges, using a zig-zag stitch, preventing unravelling of the fabric edges. Subsequently, two straight stitches, with width $w_a = 2.5$ cm between, are sewn down the center of the sleeve, forming the pocket for the bladder. The width w_a is chosen to allow the bladder assembly to be pulled through the sleeve.

In the next fabrication stage, the bladder is assembled, as shown in Fig. 3**B**. Two push-to-connect tube fittings (McMaster-Carr, Push-to-Connect Tube Fitting for Air/Water, Straight Adapter, 5/32” Tube OD x 1/8 NPT Male) are inserted in both ends of a silicon tube (McMaster-Carr, Silicone Rubber Tubing, Durometer 35A, 1/4” ID, 3/8” OD) with length L_p. Next, two brass hose ferrules (Grainger, 0.700” Brass Hose Ferrule), position around the silicon tube and push-to-connect tube fittings, are crimped, uses a lever operated crimper, sealing the bladder. The push-to-connect tube fittings are easily interfaced with pneumatic tubing (McMaster-Carr, High-Pressure Nylon Tubing, 0.106” ID, 5/32” OD), e.g., on one end and a plug on the other (McMaster-Carr, Push-to-Connect Tube Fitting for Air, Plug, 5/32” Stem OD).

The last stage of fabrication (Fig. 3**C**) combines the two subassemblies by securing the bladder to the sleeve using custom 3D printed end caps. First, the bladder is inserted into the actuator sleeve. We found that first threading a steel rope through the sleeve, then using the rope to pull the bladder through is effective. The end caps are designed to encapsulate the sleeve and cylindrical hose ferrules (at the ends of the bladder), preventing the bladder from escaping the sleeve. The end caps are secured together using socket head screws (McMaster-Carr, M3x0.5mm Thread, 10mm Long) and hex nuts (McMaster-Carr, M3x0.5mm Thread). Note that, before the end caps are installed, holes are punch through the sleeve. The holes allow the screws through the sleeve, and accommodate a zip-tie, installed last, providing increased support at the distal ends of the end caps.

C. Pressure Control

The internal pressure P_m of a single fabric-based helical actuator is maintained at a desired pressure P_d using on-off control of two solenoid valves (SMC, SY113-SMO-PM-F), one valve connected to an air reservoir (maintained at 860 kPa (125 psi)), and the other an exhaust valve. A block diagram illustrating the controller architecture is depicted in Fig. 4. Internal pressure of the actuator is measure with a piezoresistive silicon pressure sensor (Honeywell, HSC-

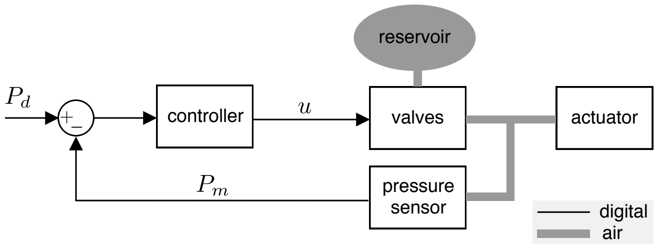

Fig. 4: Single actuator control architecture. The goal is to maintain the actuator's internal pressure P_m at the desired pressure P_d. The controller block updates valve signal u according to (1).

SANN150PG2A3), connected to the actuator with pneumatic tubing. The controller determines the state u of the valves as follows:

$$u = \begin{cases} 1 & \text{if} \quad P_d - P_m > 0 \\ 0 & \text{if} \quad -\bar{e} \leq P_d - P_m \leq 0 \\ -1 & \text{if} \quad P_d - P_m < -\bar{e} \end{cases} \tag{1}$$

where the interval $[-\bar{e}, 0]$ is the deadband, and $u = 1$ the solenoid valve connected to the reservoir is on (i.e., open), $u = -1$ the exhaust solenoid valve is on, and when $u = 0$ both valves are off (i.e., remain closed). The deadband, reduces high frequency valve switching and is selected as $\bar{e} = 14$ kPa (2 psi). The control loop, implemented on a BeagleBone Black (REV C.) development platform with custom software, has a loop frequency of 1 kHz.

D. Experimental evaluations

To investigate the effect of knit angle ϕ on the actuator mechanics, three actuators were constructed with knit angles $\phi = [15°, 30°, 45°]$. While fixed at one end, each actuator was pressurized from 0 kPa to 828 KPa (120 psi) in increments of 138 kPa (20 psi). The sequence of pressurized states for each actuator is shown in Fig. 5. As the knit angle ϕ is increased, the winding radius decreased and pitch length (distance between successive windings) increased (see Fig. 5), consistent with elastomer-based helical actuators [17]. Note that positive values of ϕ correspond to right-handed helices.

The torque characteristic of each actuator (i.e., with knit angle $\phi = [15°, 30°, 45°]$) was empirically evaluated by isometrically constraining the actuator, gradually pressurizing/depressurizing (i.e., as a staircase function), and measuring the magnitude of generated torque with a multi-axis force/torque sensor (ATI Industrial Automation, Model Delta). The experimental setup is illustrated in Fig. 6. The results indicate that as knit angle ϕ increased, the magnitude of achieved torque (i.e., about the x-axis in Fig. 6) increased. This can be seen in Fig. 7, which shows the magnitude of torque versus internal pressure for each actuator. The results indicate a negligible amount of hysteresis between inflating/deflating, and that torque is well approximated by a linear dependence on pressure. The maximum torques, at an inflation pressure of $\sim$700 kPa (100 psi), were approximately 0.45 Nm, 0.82 Nm, and 1.7 Nm, for knit angles 15°, 30° and 45°, respectively.

The controller performance was characterized with a step response using the setup described above (Fig. 6) and the actuator with knit angle $\phi = 45°$. The internal pressure P_m and actuator torque τ were measured simultaneously, while the desired pressure P_d was set to 620 kPa (90 psi) for 5 seconds. The pressure P_m and torque τ responses can be seen in Fig. 8. The torque time constant was estimated from Fig. 8 as $\tau_{ts} = 0.67$, (i.e., the time to reach 63% of steady state), corresponding to a approximate bandwidth of 0.24 Hz, which is consistent with similar control approaches [6].

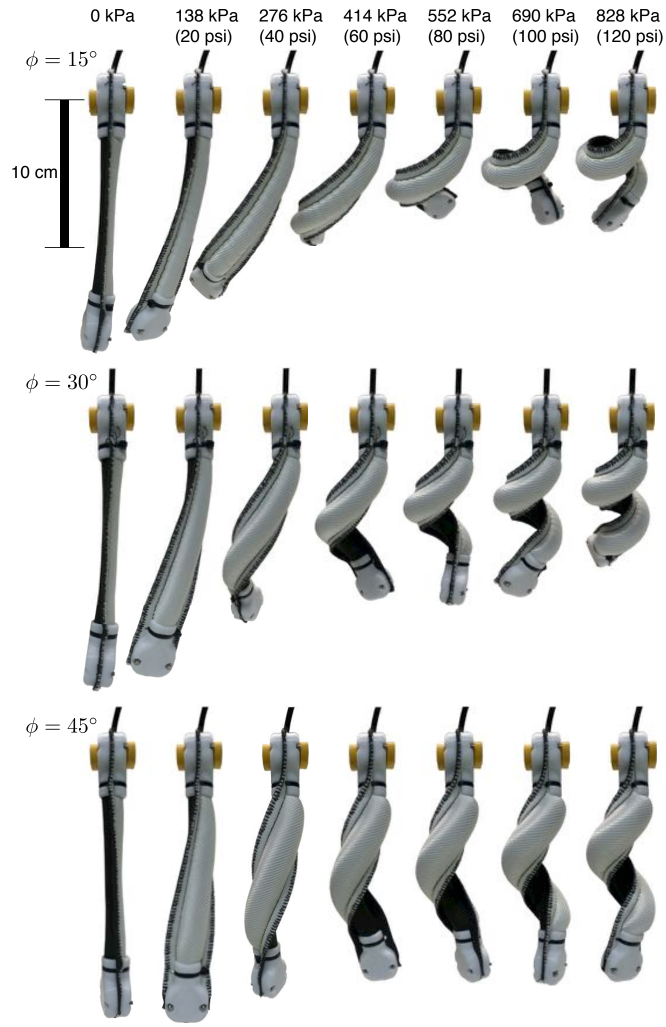

Fig. 5: Series of inflation pressures for actuators with different knit angles (ϕ). Each column represents a different inflation pressure.

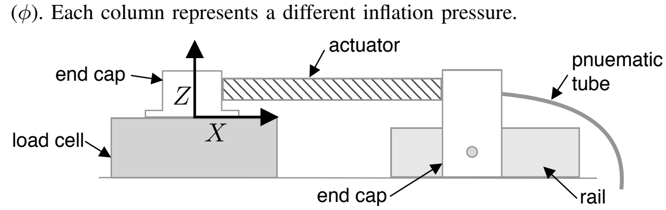

Fig. 6: Side view schematic of experimental setup. The actuator is held isometrically with one end attached to a load cell.

III. Robotic Orthosis Design and Fabrication

Practical consideration for the design of the robotic orthosis include comfortability, sufficient torque assistance, and ease of donning/doffing. The challenges are to physically attaching the device to the user, and adequately transmit the assistive torques.

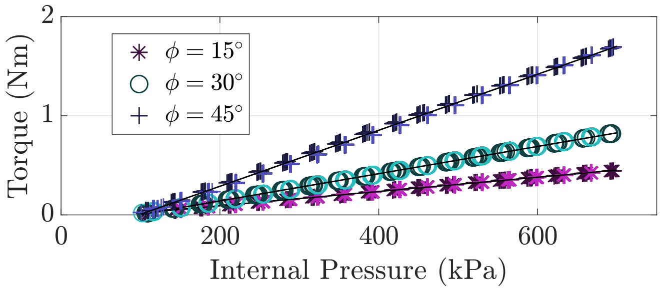

Fig. 7: Scatter plot of torque versus pressure data, for each knit angle ϕ, during isometric experiments. Dark markers denote loading (increasing pressure), and light markers denote unloading (decreasing pressure). Solid lines are linear fits.

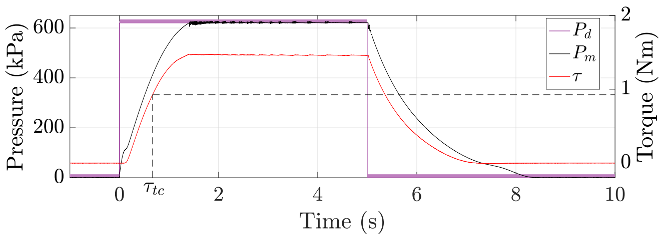

Fig. 8: Step response for a single actuators. Note that the desired pressure P_d is shown with the deadband (see (1)), and the torque scale for τ is located on the right hand side, and the horizontal dashed line represents 62.3% of steady state torque value. The time constant τ_{tc} is denoted by the vertical dashed line.

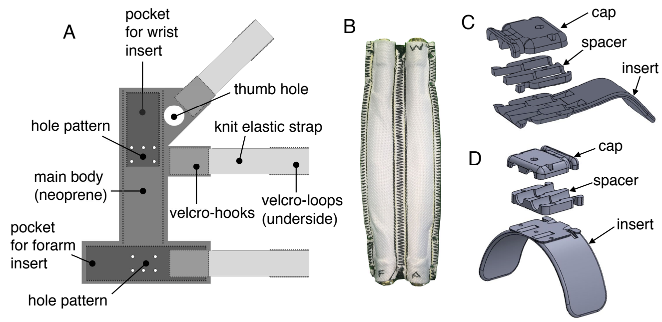

Fig. 9: Components of the robotic wrist orthosis. (**A**) Neoprene sleeve with pockets for support inserts, and elastic straps. (**B**) Antagonist fabric-based helical actuators fabricated with a single strain-limiting base layer. (**C**) Exploded view of wrist support structure. (**D**) Exploded view of the forearm support structure.

The proposed solution is a sleeve (Fig. 9**A**), incorporating an antagonistic pair of fabric-based helical actuators (Fig. 9**B**) secured though strategically placed rigid support structures (Fig. 9**C**-**D**). The palmar side of the sleeve is constructed from neoprene (Vogue Group Inc, 1.5mm Neoprene Scuba Black), and features of a thumb hole, pockets for the rigid inserts, hole patterns for securing the rigid insert and actuators, and three elastic straps with velcro. The dorsal side of the sleeve is lycra (Richland Textiles, Nylon Lycra Spandex Raschel Black).

Maximum biological torque is approximately 7.4 Nm and 5.5 Nm for pronation and supination, respectively [18], therefore, the helical actuators with $\phi = 45°$, which can produce up to 1.7 Nm are used. The same process outline in Sect. II-B is used to construct the antagonistic pair of helical actuators (Fig. 9**B**), with the only difference being that two anisotropic patterns, one with $\phi = 45°$ (producing a right helix when inflated) and the other with ϕ = -45° (producing a left helix when inflated), are sewn on a single strain-limiting layer.

The prototype design is inspired by commercial wrist braces, which typically utilize a rigid member that extends from the distal end of the wrist to the center of the palm. In the case of the proposed device, the support structures have two functions: (1) attaching the actuators to the sleeve, and (2) transmitting the generated torques. The wrist support structure, shown in Fig. 9**C**, consist of a supporting insert (ergonomically shaped to fit the wrist and palm), a spacer, and cap. The design is a modified version of the 3D printed end caps (e.g., see Sect. II-B), but incorporates a wrist/palm support structure. During assembly, the wrist insert is placed inside the wrist pocket of the sleeve. The spacer provides a cylindrical region for the fabric-based actuators. Next, the cap is placed on top and screws/nuts secure the assembly. The forearm support structure, ergonomically shaped for the forearm, is identically assembled.

To don the device, the user inserts their hand through the sleeve, then fastens the elastic velcro straps, which are situated such that the straps secure the rigid wrist and forearm supports (see Fig. 1). The total weight of the device is approximately 200 g, not including the control system (CPU, valves and sensors), or reservoir tank.

IV. Experimental Evaluation

A. Overview

Six healthy subjects (4 men, 2 women) were recruited to participate in the experiment accessing the assistive torque capabilities of the robotic forearm orthosis. The subjects completed two reaching tasks, one for pronation and one for supination, where the goal was to rotate and hold a handle at a pre-determined target. We hypothesize that an increase in assistive torque supplied by the robotic orthosis would decrease user effort.

The experimental setup, shown in Fig. 6, consisted of a grip handle with the axis of rotation aligned to that of the user's forearm rotation. The handle was attached to the shaft of a rotary hall-effect sensor (TT Electronics, 6127 V1 A360 L.5 FS), which was mounted in the handle base and provided angular position measurements. A torsional spring (McMaster-Carr, 9271K693 and 9271K627), with spring constant K = 0.02 Nm/deg, placed in between the base and the grip handle, provided rotational resistance. The neutral position of the spring corresponded to neutral pronation/supination (i.e., handshake position). The handle base and elbow support were attached to railing (secured to a table), and could be adjusted. A circular target board, located behind the handle base and in the line of sight of the subject, had two marked targets at approximately θ_d = 45° (supination target) and θ_d = -50° (pronation target), as measured from vertical. Surface electromyography (sEMG) sensors (Biometrics Ltd, SX230-1000) and an sEMG datalogger (Biometrics Ltd, DataLog MWX8), were used to record muscle activity of the bicep and pronator teres,

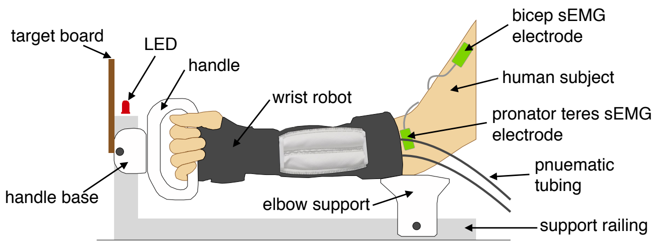

Fig. 10: Side view schematic of the pronation/supination assistance evaluation experimental setup with major components labeled.

which have been shown to correlate well with supination and pronation, respectively [19]. An LED was used to indicate the beginning/ending of a trial. The signals for the rotary hall-effect sensor, LED indicator, and robotic orthosis were handled by the custom embedded system (i.e., BeagleBone Black) and synced with the sEMG signals, both sampled at 1 kHz.

B. Protocol

Following sEMG placement, data during maximum voluntary contraction (MVC) were collected. Then, after donning the robotic orthosis, it was activated to the maximum assistance (1.5 Nm) in both pronation and supination direction, allowing the subject to become familiar with the device. Next, the subject was seated next to the apparatus, with their right arm configured as in Fig. 6. Supination and pronation were tested independently, with identical protocols, as follows. There were four ordered condition blocks: baseline, low torque (0.3 Nm), medium torque (0.9 Nm), and high torque (1.5 Nm) assistance. During each block, the subject completed five reaching trials. The goal was to rotate the handle until it aligned with the target, and hold the handle at the target for five seconds. Each trial was initiated by the LED indicator, which remained on for five seconds, with a pause of five seconds before the next trial begun. After each block the subject rested. During the testing blocks with torque assistance, the robotic orthosis was pressurized at the start of each trial (i.e., synchronized with the LED indicator), according to the torque-pressure linear relationship (see Fig. 7).

C. Data analysis

Linear envelopes of raw sEMG signals were calculated by full wave rectifying the signals, then low-pass-filtering (first order, zero phase, cutoff frequency of 3 Hz). For each trial, the subject's effort was quantified as the root-mean-square (RMS) of the linear envelope sEMG, normalized by the maximum of the linear envelope sEMG during MVC. The task error for each trial was quantified as the RMS difference of the desired angular position and actual angular position. To ensure steady-state behavior, only the last two seconds of each trial were analyzed. Statistical analysis consisted of fitting a linear mixed-effects model to evaluate the influence of torque assistance (fixed-effects) on the level of effort and task error (outcome measures), with participants treated as a random effect.

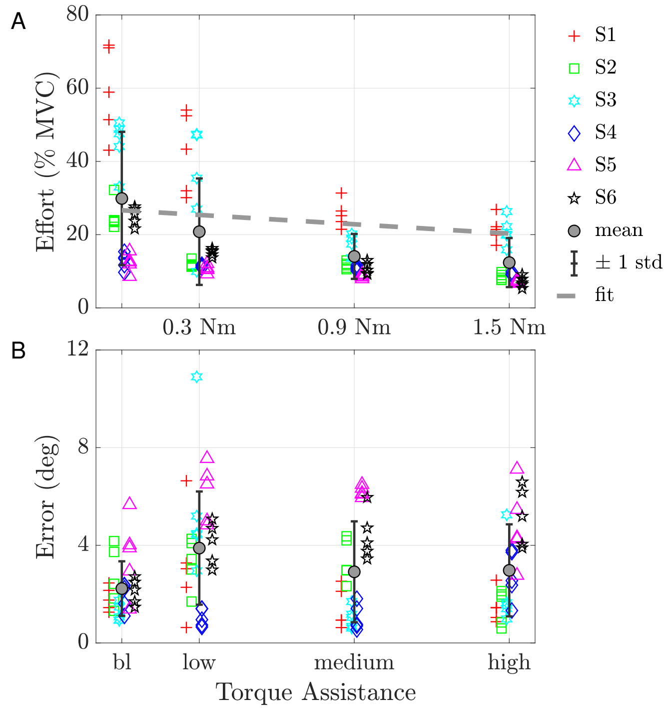

Fig. 11: Results from the supination task: scatter plot of subjects' (**A**) effort, and (**B**) task error, for all trials and assistance levels (note bl=baseline, i.e., no assistance). Group mean ($\pm$1 std) is denote with solid circles (error bars). Dashed line represents linear fit from the mixed-effects model.

D. Results

Subjects' effort during the supination experiment, for each trial and assistance level (bl=baseline, low, medium, high), are shown in Fig. 11**A**, and corresponding task errors are shown in Fig. 11**B**. The assistive torque significantly decreased subjects' bicep activation, i.e., effort, (slope = -10.995 (% MVC/Nm), 95% confidence interval -13.378 to -8.6124, p<3e-15), while not significantly affecting the task error (slope $= 0.112$ (deg/Nm), $p \approx 0.7$). On average, high torque assistance (1.5 Nm) decreased effort by 59%, from a group mean of 29% MVC during the baseline condition to a group mean 12% MVC during the high torque assistance condition. The mean effort of each subject progressively decreased from baseline to high assistance, except subject S3's effort, which increased slightly from the medium torque assistance (17% MVC) to the high assistance (21% MVC). Most subjects achieved the lowest error during the baseline condition, however, there was no significant statical trend.

Subjects' effort during the pronation task are shown in Fig. 11**A**, with task error shown in Fig. 11**B**. The assistive torque significantly decreased subjects' effort (slope = -4.2431 (% MVC/Nm), 95% confidence interval -6.1926 to -2.2936, p<4e-5). Again, the task error was not significantly influenced by the level of assistance (slope $= 0.28661$ (deg/Nm), $p \approx 0.1$). On average, high torque assistance (1.5 Nm) decreased effort by 24%, from a group mean of 27% MVC during the baseline condition to a group mean 21% MVC during the high torque assistance condition. The mean effort of most subjects progressively decreased from baseline to high assistance. The exceptions being subject S2, mean effort increased slightly from the baseline condition (22%

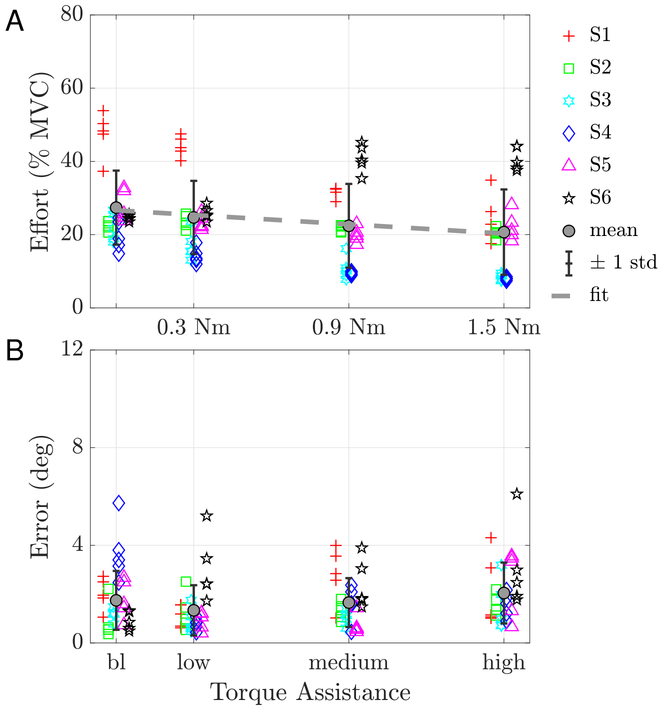

Fig. 12: Results from the pronation task: scatter plot of subjects' (**A**) effort, and (**B**) task error, for all trials and assistance levels (note bl=baseline, i.e., no assistance). Group mean (± 1 std) is denote with solid circles (error bars). Dashed line represents linear fit from the mixed-effects model.

MVC) to the low assistance (24% MCV), subject S4, mean effort increased slightly from the medium torque assistance (20% MVC) to the high assistance (22% MVC), and S5, mean effort progressively increased.

V. Discussion

Effort for nearly all individuals reduced with increased assistance. However, the effect was more apparent in some subjects. Referring to Fig. 11**A**, which shows effort during the supination task, it can be seen that subject S1 obtained the most benefits, while subjects S4 and S5 received the least. This is most likely due to a *floor effect*: the baseline task might have been to easy for some subjects. Future studies will take this into account by customizing the resistance to the user. Additionally, future studies should include both healthy and people with impairments, as well as randomized conditions.

The robotic orthosis provided more useful assistance in supination than during pronation, evident by a larger decrease in effort. A potential explanation is that, since the pair of actuators were attached along the palmar side of the arm, during supination the device is effectively *pushing* the user, while in pronation the device is *pulling* the user (see Fig. 1). The act of *pulling*, due to the nature of the attachments, may be suboptimal at torque transmission. Future embodiments will explore alternative actuator routing. Additionally, increased bandwidth, miniaturizing, and structural modeling of the actuators are critical for future development.

VI. Conclusion

This work presented a preliminary investigation of a robotic forearm orthosis, utilizing fabric-based helical actuators. The helical actuators were shown to achieve a substantial fraction of biological forearm pronation torque. A prototype orthosis, utilizing the fabric-based actuators was fabricated. An experimentally assessement, with healthy subjects ($N = 6$), showed that subjects' effort could be decreased by an average of 59% and 24% during supination and pronation, respectively. This work demonstrates that fabric-based helical actuators are a viable technology for creating assistive wearable robots, motivating future investigation.

References

[1] B. Morrey, L. Askew, E. Chao *et al.*, "A biomechanical study of normal functional elbow motion," *J. Bone Joint Surg. Am.*, vol. 63, no. 6, pp. 872–7, 1981.

[2] P. Maciejasz, J. Eschweiler, K. Gerlach-Hahn, A. Jansen-Troy, and S. Leonhardt, "A survey on robotic devices for upper limb rehabilitation," *J. NeuroEng. Rehabil.*, vol. 11, no. 1, p. 3, 2014.

[3] N. Jarrasse and G. Morel, "Connecting a human limb to an exoskeleton," *IEEE Trans. Robot.*, vol. 28, no. 3, pp. 697–709, 2012.

[4] J. Laut, M. Porfiri, and P. Raghavan, "The present and future of robotic technology in rehabilitation," *Curr. Phys. Med. Rehabil. Rep.*, vol. 4, no. 4, pp. 312–319, 2016.

[5] D. Chiaradia, M. Xiloyannis, C. W. Antuvan, A. Frisoli, and L. Masia, "Design and embedded control of a soft elbow exosuit," in *2018 IEEE Int. Conf. on Soft Robotics*. IEEE, 2018, pp. 565–571.

[6] P. Polygerinos, Z. Wang, K. C. Galloway, R. J. Wood, and C. J. Walsh, "Soft robotic glove for combined assistance and at-home rehabilitation," *Rob. and Auton. Syst*, vol. 73, pp. 135–143, 2015.

[7] T. H. Koh, N. Cheng, H. K. Yap, and C.-H. Yeow, "Design of a soft robotic elbow sleeve with passive and intent-controlled actuation," *Front. Neurosci.*, vol. 11, p. 597, 2017.

[8] N. W. Bartlett, V. Lyau, W. A. Raiford, D. Holland, J. B. Gafford, T. D. Ellis, and C. J. Walsh, "A soft robotic orthosis for wrist rehabilitation," *J. Med. Dev.*, vol. 9, no. 3, p. 030918, 2015.

[9] F. Connolly, P. Polygerinos, C. J. Walsh, and K. Bertoldi, "Mechanical programming of soft actuators by varying fiber angle," *Soft Rob.*, vol. 2, no. 1, pp. 26–32, 2015.

[10] T. Wang, L. Ge, and G. Gu, "Programmable design of soft pneu-net actuators with oblique chambers can generate coupled bending and twisting motions," *Sens. and Actuators A-Phys.*, vol. 271, pp. 131–138, 2018.

[11] S. Sanan, P. S. Lynn, and S. T. Griffith, "Pneumatic torsional actuators for inflatable robots," *J. of Mech. Rob*, vol. 6, no. 3, p. 031003, 2014.

[12] C. R. Nesler, T. A. Swift, and E. J. Rouse, "Initial design and experimental evaluation of a pneumatic interference actuator," *Soft robotics*, vol. 5, no. 2, pp. 138–148, 2018.

[13] C. S. Simpson, A. M. Okamura, and E. W. Hawkes, "Exomuscle: An inflatable device for shoulder abduction support," in *2017 IEEE Int. Conf. on Robotics and Automation,*. IEEE, 2017, pp. 6651–6657.

[14] J. Chung, R. Heimgartner, C. T. O'Neill, N. S. Phipps, and C. J. Walsh, "Exoboot, a soft inflatable robotic boot to assist ankle during walking: Design, characterization and preliminary tests," in *2018 7th IEEE Int. Conf. on Biomedical Robotics and Biomechatronics*. IEEE, 2018, pp. 509–516.

[15] C. T. O'Neill, N. S. Phipps, L. Cappello, S. Paganoni, and C. J. Walsh, "A soft wearable robot for the shoulder: Design, characterization, and preliminary testing," in *Rehabilitation Robotics (ICORR), 2017 International Conference on*. IEEE, 2017, pp. 1672–1678.

[16] L. Cappello, K. C. Galloway, S. Sanan, D. A. Wagner, R. Granberry, S. Engelhardt, F. L. Haufe, J. D. Peisner, and C. J. Walsh, "Exploiting textile mechanical anisotropy for fabric-based pneumatic actuators," *Soft Rob.*, 2018.

[17] W. Hu, W. Li, and G. Alici, "3d printed helical soft pneumatic actuators," in *2018 IEEE/ASME Int. Conf. on Advanced Intelligent Mechatronics*. IEEE, 2018, pp. 950–955.

[18] J. Matsuoka, R. A. Berger, L. J. Berglund, and K.-N. An, "An analysis of symmetry of torque strength of the forearm under resisted forearm rotation in normal subjects," *J. Hand Surg. Am.*, vol. 31, no. 5, pp. 801–805, 2006.

[19] J. Bader, M. R. Boland, D. Greybe, A. Nitz, T. Uhl, and D. Pienkowski, "Muscle activity during maximal isometric forearm rotation using a power grip," *J. Biomech*, vol. 68, pp. 24–32, 2018.